

Conservative limits on primordial black holes from the LIGO-Virgo-KAGRA observations

Mehdi El Bouhaddouti,^{1,*} Muhsin Aljaf,^{1,†} and Ilias Cholis^{1,‡}

¹*Department of physics, Oakland University, Rochester Michigan, 48309,U.S.A*

Primordial black holes (PBH) may constitute a considerable fraction of dark matter. In this work we use the recent observations by the LIGO-Virgo-KAGRA (LVK) collaborations to set direct limits on stellar-mass range PBHs. We evaluate the merger rates of PBH binaries by accounting for the binaries formed by two-body captures inside dark matter halos and by studying the evolution of PBH binaries inside such halos through binary-single interactions. Those type of interactions contribute to what is a minimum of PBH merger rates at low redshifts detectable by LVK. Thus, they allow us to derive what is the most conservative upper limits on the presence of merging PBH binaries in the gravitational-wave observations. We study both the case where PBHs have a monochromatic mass-distribution and the case where that distribution is described by a log-normal function. To derive limits on PBHs, we simulate binaries with masses following the relevant mass-distributions and merger rates as a function of redshift, up to $z \sim 0.8$, relevant for the current LVK observations. In those simulations we also take into account that the LVK observatories measure the detected black hole binaries' masses with a finite resolution. In comparing to the LVK observations, we combine the simulated PBH binaries with the binaries following a power-law mass- and redshift-distribution. The latter binaries dominate the observed population of LVK detections. Our derived limits on the mass fraction of dark matter composed of PBHs is in the range of 10^{-3} to $O(1)$, depending on the exact assumptions relating to the PBH binaries properties. For reasonable assumptions on those PBH binaries' properties before their evolution inside dark matter halos, we get that fraction to be in the range of $5 \times 10^{-3} - 0.1$, for PBH masses of 5-80 M_{\odot} . Our limits even with a conservative choice on evaluating the low-redshift merger rates provide some of the most competitive limits in the mass range of 5-40 M_{\odot} .

I. INTRODUCTION

The nature of dark matter remains one of the most fundamental open questions in cosmology and particle physics. Candidates, in mass, span many orders of magnitude, ranging from 10^{-22} eV to $O(10^3)M_{\odot}$ [1, 2]. The highest-end of the dark matter candidates' mass range, is occupied by primordial black holes (PBHs), generated from the collapse of early universe curvature perturbations [3–5]. With the current generation of ground-based gravitational-wave (GW) observatories we have the opportunity, for the first time to directly probe PBHs with masses $\gtrsim 1M_{\odot}$, through the merger of PBH binaries leaving a signal at the LIGO-Virgo-KAGRA (LVK) interferometers [6–11].

The most direct manner by which we can probe a signal of PBHs in the LVK observations is through the mass-distribution of the detected events containing black holes (BHs) and other compact objects [12–14]. These include studying either only the individual masses of the observed BHs [15, 16], or the combined information of the binaries' masses [12, 17, 18]. In the latter case, one cares also on how correlated the values of the primary mass of the binary M_1 is to the secondary mass of the binary M_2 ; as

that may provide a manner to separate the process by which these binaries have formed (see e.g. [12, 16, 19–22]). Alternative probes/signals of a PBH component in the GW observations have also been proposed in [23–29].

PBH binaries may form in multiple pathways. One path is through, GW direct captures, which happens when two unbounded PBHs come that close to emit enough GW energy to form a highly-eccentric binary that would merge soon after [6]. Another pathway, is via interactions occurring between PBH binaries and single PBHs within the dark matter halos (for a recent analysis see [30, 31]). Finally, PBH binaries may form from the early universe perturbations and evolve slowly through GW emission to merge in our time without interacting substantively with their environments [7, 32].

In this paper, we use the LVK observations from observing runs 1 (O1) to 3 (O3), to place limits on the abundance of PBHs. We describe those in terms of the fraction dark matter density in PBHs, f_{PBH} , where $\rho_{\text{PBH}} = f_{\text{PBH}} \cdot \rho_{\text{DM}}$. In Sec. II, we describe our calculations of the PBH merger rates under assumptions on their initial abundance, the fraction of PBH in binaries and their mass distribution. To derive our limits in Sec. III, we rely on the method of representing the O1-O3 LVK observations presented in [33]. We place limits on PBHs, first under the assumption that they have a monochromatic mass-distribution, with that mass being a free parameter. We find that the O1-O3 LVK limits set some of the most robust and tight limits in the mass range of 3 to 40 M_{\odot} , with $2 \times 10^{-2} < f_{\text{PBH}} < 10^{-1}$. We also study the assumption that PBHs follow a log-

* melbouhaddouti@oakland.edu, ORCID: orcid.org/0009-0001-1299-0879

† muhsinaljaf@oakland.edu, ORCID: orcid.org/0000-0002-1251-4928

‡ cholis@oakland.edu, ORCID: orcid.org/0000-0002-3805-6478

normal mass-distribution [34, 35]. Our limits for the log-normal distribution are also the most competitive among the various probes; between 3 and $40 M_\odot$, we get $1 \times 10^{-2} < f_{\text{PBH}} < 10^{-1}$. Alternative mass distributions for the PBHs have been proposed as in [36–40] give similar limits. We conclude in Sec. IV and discuss future improvements in probing for a PBH signal in the black hole mass distribution with upcoming GW observations.

II. THE MERGER RATES OF PRIMORDIAL BLACK HOLES

A. Monochromatic primordial black holes

In this work we consider that PBHs exist both as single objects and in binaries with other PBHs. The fraction of PBHs in binaries is $0 < f_{\text{PBH binaries}} < 1$. For a given dark matter halo or virial radius R_{vir} , the direct PBH capture rate is [6, 31],

$$\Gamma_{\text{capture}} = 2\pi \int_0^{R_{\text{vir}}} r^2 \langle \sigma \cdot v_{\text{PBH}} \rangle \frac{[f_{\text{PBH}} \cdot \rho_{\text{NFW}}(r)]^2}{m_{\text{PBH}}^2} dr, \quad (1)$$

where σ is the cross-section for direct captures [41, 42], m_{PBH} is the PBH mass, v_{PBH} is relative velocity between them and ρ_{NFW} is density profile of the dark matter halo. We assume that all dark matter halos follow the Navarro, Frenk and White (NFW) density profile [43]. Given the cosmologically short interval between the creation of these binaries via captures and the binaries' mergers, this leads to the merger rate per halo, $R_{\text{halo}}(M, z)$, given by,

$$R_{\text{halo}}(M, z) = \frac{2\pi}{3} \left(\frac{85\pi}{6\sqrt{2}} \right)^{2/7} f_{\text{PBH}}^2 \quad (2) \\ \times \frac{G^2 \cdot [M_{\text{vir}}(z)]^2 \cdot D_v(z) \cdot f(C(z))}{[R_s(z)]^3 \cdot c \cdot [g(C(z))]^2}.$$

$M_{\text{vir}}(z)$, is the virial mass of a given dark matter halo at redshift z with a scale radius $R_s(z)$. $D_v(z)$ is related to the velocity distribution of PBHs inside halos. $C(z)$ is the redshift-dependent concentration parameter of dark matter halos, and $g(C(z))$ and $f(C(z))$ are relevant functions (see for more details [31]). The total rate is then calculated as,

$$R_{\text{total}}(M, z) = \int R_{\text{halo}}(M, z) \frac{dn}{dM} dM, \quad (3)$$

where dn/dM is the halo mass function. We use the Press-Schechter halo mass function [44] and consider dark matter halos in the mass range of $10^3 - 10^{15} M_\odot$. A detailed calculation for the case where the PBHs follow a continuous mass-distribution is provided in Ref. [31]. We note that for direct captures, the merger rates depend only on f_{PBH} and not on $f_{\text{PBH binaries}}$ [31].

Ref. [31], studied the interactions between PBH binaries and single PBHs in dark matter halos. Through such

interactions, hard binaries get harder. The frequency of this process depends on the density and the dispersion velocity of halos, which in turn depends on location within each halo and the halo's evolutionary stage. As shown in [31], the resulting merger rates can be dominant over the direct capture rates.

Following Ref. [31], we simulate a given halo by partitioning it in up to ten mass shells and evolve them in time starting from a redshift of 12. This allows us to properly account for the position- and time-dependence of the dispersion velocity v_{disp} of the PBHs and their density that is proportional to ρ_{NFW} . This allows us to evolve the orbital properties of the PBH binaries inside the halos through,

$$\frac{da}{dt} = - \frac{G \cdot H \cdot \rho_{\text{env}}(r, t)}{v_{\text{disp}}^{\text{env}}(r, t)} a^2 - \frac{64}{5} \frac{G^3}{c^5 a^3} \cdot f(m) \cdot F(e) \quad (4)$$

$$\frac{de}{dt} = \frac{G \cdot H(r, t) K(r, t) \cdot \rho_{\text{env}}(r, t)}{v_{\text{disp}}^{\text{env}}(r, t)} a \\ - \frac{304}{15} \frac{G^3}{c^5 a^4} \cdot f(m) \cdot D(e), \quad (5)$$

with $f(m) = (m_1 + m_2)(m_1 \cdot m_2)$ and $F(e)$ and $D(e)$ being functions of the eccentricity of the binary. The ρ_{env} and $v_{\text{disp}}^{\text{env}}$, are to indicate that for all binaries we keep track of their environment's evolution (i.e. mass shell) from redshift of 12 to 0. If at any time step of our simulations, the semi-major axis a approaches zero, we consider that binary to be merging. In this manner we evaluate the merger rate per halo of a given mass, at a given time. To get the total PBH merger rate from binary-single interactions for the entire range of dark matter halos at a given redshift, we use again Eq. (3).

Ref. [31], provides for monochromatic $30 M_\odot$ PBHs, all details on the calculation of the total merger rate due to direct captures and due to binary-single interactions. In this work we expand our calculations to study PBHs in the mass range of $5 - 80 M_\odot$. In performing the same type of simulations in this work, we have found the following rescaling formula on the total merger rates to be valid,

$$R_{\text{total}}(z, m_{\text{PBH}}) = \int_{M_{\text{min}}}^{M_{\text{max}}} R_{\text{halo}, 30}(z, M) \\ \times s(m_{\text{PBH}}, M) \frac{dn}{dM} dM. \quad (6)$$

Where $R_{\text{total}}(z, m_{\text{PBH}})$ is the total merger rate for monochromatic PBHs of mass m_{PBH} , at redshift z . $R_{\text{halo}, 30}(z, M)$ denotes the total merger rate at redshift z for PBHs with a mass of $30 M_\odot$ in a halo of mass M [31]. The rescaling function $s(m_{\text{PBH}}, M)$ is,

$$s(m_{\text{PBH}}, M) = \left(\frac{30 M_\odot}{m_{\text{PBH}}} \right)^{\gamma(M)} \quad (7)$$

and the exponent γ was found based on our simulations to be empirically,

$$\gamma(M) = \delta \cdot M^\epsilon, \quad (8)$$

with $\delta = 1.18$ and $\varepsilon = -0.14$ ¹. In Fig. 1, for the monochromatic case we show the dependence of the γ exponent of Eqs. (7) and (8), to the halo's mass M (on the left y -axis), as well as the dependence of the rescaling function $s(m_{\text{PBH}}, M)$ on M (on the right y -axis). For $s(m_{\text{PBH}}, M)$ we show results for $m_{\text{PBH}} = 10 M_{\odot}$ and $60 M_{\odot}$.

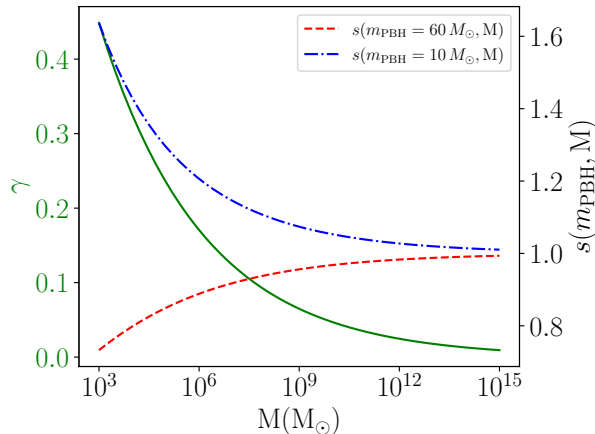


FIG. 1. The dependence of the rescaling function $s(m_{\text{PBH}}, M)$ and its γ exponent with dark matter halo mass. As the $s(m_{\text{PBH}}, M)$ depends also on the PBH mass m_{PBH} we show its dependence for two PBH masses: $10 M_{\odot}$ (blue dash-dotted) and $60 M_{\odot}$ (red dashed).

Fig. 2 depicts the total merger rate of PBH binaries, at $z = 0$, as a function m_{PBH} for the monochromatic distribution (blue solid line). Moreover, as the direct capture rate is independent of m_{PBH} , the dependence of the total rate on m_{PBH} originates from binary-single interactions of PBHs. Their rate is independent of m_{PBH} in the very massive dark matter halos. However, in low-mass halos where most of such mergers occur, there is dependence on m_{PBH} . In the following we describe why that is the case.

The rate of PBH binary-single interactions per halo mass per volume is given by,

$$R = n_{\text{hard-binaries}} \cdot n_{\text{single PBH}} \cdot \sigma_{\text{binary-single}} \cdot v_{\text{disp}}. \quad (9)$$

$n_{\text{single PBH}}$, is the number density of single PBHs (including PBHs in wide binaries) and $\sigma_{\text{binary-single}}$ is the interaction cross-section of PBH binaries with other PBHs. The number density of hard binaries is $n_{\text{hard-binaries}} = f_{\text{hard}} \cdot n_{\text{PBH binaries}}$, where $n_{\text{PBH binaries}}$ is the density of PBH binaries and f_{hard} the fraction of them that are hard, i.e. the PBH binaries with a semi-major a below

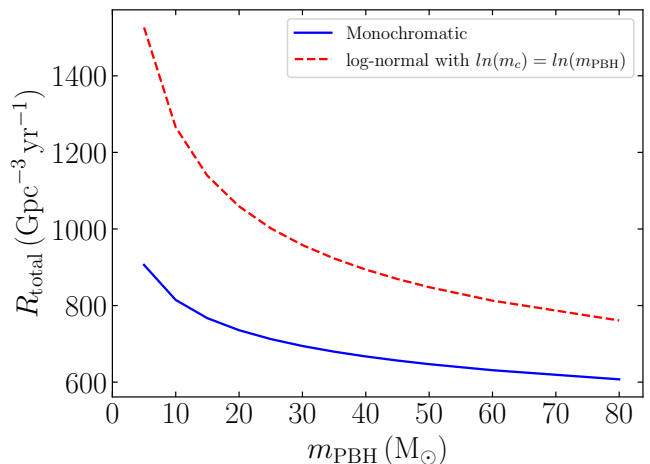


FIG. 2. The total merger rate of PBH binaries at $z = 0$, due to two body captures and binary-single interactions as a function of m_{PBH} . The blue solid line gives the rate for a monochromatic distribution. The red dashed line gives instead the rate for a log-normal mass distribution with $\mu \equiv \ln(m_c) = \ln(m_{\text{PBH}})$ and $\sigma = 0.6$.

the critical value of,

$$a_h(r, t) = \frac{G m_{\text{PBH}}}{4v_{\text{disp}}(r, t)^2}. \quad (10)$$

Only (hard) binaries with $a < a_h$, will merge within the Hubble time. This criterion is environment-dependent due to $v_{\text{disp}}(r, t)$, the dispersion velocity of the dark matter halo that the PBHs are in. Eq. (10) for $a_h(r, t)$ shows that a_h increases linearly with the mass of m_{PBH} . In massive halos, the dispersion velocity $v_{\text{disp}}(r, t)$ is high and only a small fraction of the PBH binaries are hard. In fact, in the very massive halos we find that approximately, $f_{\text{hard}} \propto m_{\text{PBH}}$. However, in the smallest dark matter halos $M \sim 10^3 M_{\odot}$, almost all PBH binaries are hard, i.e. $f_{\text{hard}} \simeq 1$. In Appendix A, we provide further details on how the environments the PBH binaries are in, affect the ratio f_{hard} .

For a given value of semi-major axis, the cross-section for PBH binary-single interaction scales with m_{PBH} ,

$$\sigma_{\text{binary-single}} = \frac{2\pi G \cdot (3 m_{\text{PBH}}) \cdot a}{v_{\text{disp}}^2} \propto m_{\text{PBH}}. \quad (11)$$

Combining all those dependencies on m_{PBH} , we find from Eq. (9), that in large halos, the PBH binary-single interaction rate per halo is,

$$\begin{aligned} R_{\text{halo}} &\propto \left(\frac{\rho_{\text{NFW}}}{2m_{\text{PBH}}} \right) \cdot m_{\text{PBH}} \cdot \left(\frac{\rho_{\text{NFW}}}{m_{\text{PBH}}} \right) \cdot m_{\text{PBH}} \\ &\propto \text{independent to } m_{\text{PBH}}. \end{aligned} \quad (12)$$

However, in the low mass halo limit, the same PBH

¹ For PBHs with a log-normal mass distribution, we follow the same prescription of Eqs (6),(7) and (8), with $\delta = 1.25$ and $\varepsilon = -0.10$ instead.

binary-single interaction rate per halo is approximately,

$$\begin{aligned} R_{\text{halo}} &\propto \left(\frac{\rho_{\text{NFW}}}{2m_{\text{PBH}}} \right) \cdot \left(\frac{\rho_{\text{NFW}}}{m_{\text{PBH}}} \right) \cdot m_{\text{PBH}} \\ &\propto \frac{1}{m_{\text{PBH}}}. \end{aligned} \quad (13)$$

This explains the total merger rate having some dependence on m_{PBH} and the need for Eqs. (6) to (8). In practice, our simulations show that for halos with mass $M \sim 10^3 M_{\odot}$, $R_{\text{halo}} \sim 1/\sqrt{m_{\text{PBH}}}$, with increasing halo mass making the parametric dependence to m_{PBH} less sensitive. By $M \sim 10^{10} M_{\odot}$, R_{halo} is independent to m_{PBH} . The difference between the detailed simulations and the simple analytical arguments given above, is that in Eq. (11), the PBH binary-single interaction cross-section also depends on the semi-major axis a , whose critical (upper) value of what defines a hard binary also depends on m_{PBH} (see Eq. (10)).

B. Primordial black holes following a log-normal mass distribution

To simulate the merger rates for the halos made of PBHs with a mass distribution function, we take the log-normal mass distribution, defined by the probability density function,

$$\psi(m) = \frac{1}{\sqrt{2\pi} \sigma m} \exp\left(-\frac{(\ln(m) - \mu)^2}{2\sigma^2}\right), \quad (14)$$

with $\mu = \ln(m_c)$, where m_c represents the median mass (in units of M_{\odot}) and σ characterizes the width of the mass distribution.

In our simulations, when we have terms that include the mass of PBH binaries or of single PBHs as in $f(m)$, $q(m)$ and $a_h(m)$, we derive averaged values for these quantities by using the PBH mass distribution function.

The mass term $f(m)$ in the evolution equations Eqs. (4) and (5), is as follows,

$$\begin{aligned} \langle f(m) \rangle &= \int_{m_{2,\min}}^{m_{2,\max}} \int_{m_{1,\min}}^{m_{1,\max}} (m_1 + m_2)(m_1 \cdot m_2) \\ &\times \psi(m_1) \psi(m_2) dm_1 dm_2. \end{aligned} \quad (15)$$

The black hole mass ratio $q = m_2/m_1$ of binaries, for the monochromatic case is $q = 1$. For the log-normal distribution, as $m_2 < m_1$ we have,

$$\langle q(m) \rangle = \int_{m_{1,\min}}^{m_{1,\max}} \frac{1}{m_1} \psi(m_1) dm_1 \int_{m_{2,\min}}^{m_1} m_2 \psi(m_2) dm_2. \quad (16)$$

This term affects the eccentricity growth rate $K(r, t, m)$ in Eqs. (4) and (5).

At each step of our simulations, we only evolve the hard binaries. The fraction of hard binaries for a given halo mass and location within it (the spherical shell of the

halo), depends on the PBH mass distribution, through its impact on the critical value a_h ,

$$a_h(r, t) = \frac{G m_1 \cdot m_2}{4v_{\text{disp}}(r, t)^2 m_3}. \quad (17)$$

m_1 and m_2 are the masses of the PBH binary and m_3 is the mass of the interacting single PBH. Thus, for a log-normal PBH mass distribution,

$$\begin{aligned} \langle a_h(m) \rangle &= \frac{G}{4v_{\text{disp}}^2} \int_{m_{3,\min}}^{m_{3,\max}} \int_{m_{2,\min}}^{m_{2,\max}} \int_{m_{1,\min}}^{m_{1,\max}} \frac{m_1 \cdot m_2}{m_3} \\ &\times \psi(m_1) \psi(m_2) \psi(m_3) dm_1 dm_2 dm_3. \end{aligned} \quad (18)$$

In our simulations, we sample and evolve a large enough number of binaries to properly study the rare stochastic processes of direct captures and binary-single interactions. Thus, we need to properly rescale the number of studied binaries to the actual number of binaries existing in each halo mass shell i , at any given time t in the evolution of each simulated halo. For a PBH mass-distribution the actual number of PBH binaries $N_{\text{PBH binaries}, i, t}$ in a shell indexed by i at time t is approximated as,

$$N_{\text{PBH binaries}, i, t} = \frac{M_{i, t}}{4 \langle m \rangle}. \quad (19)$$

$M_{i, t}$, is the dark matter mass in PBHs in the shell i at time t . The mean PBH mass $\langle m \rangle$ is,

$$\langle m \rangle = \int_{m_{\min}}^{m_{\max}} m \psi(m) dm. \quad (20)$$

The factor of 1/4 in Eq. (19), is due to the fact that we assume $f_{\text{PBH binaries}} = 0.5$, and each binary is made up of two PBHs. The properly rescaled merger rates per halo mass is,

$$R_{\text{halo}} = \sum_{i=1}^{N_{\text{shells}}} \sum_{t=0}^{t_{\text{look}}} \frac{N_{\text{PBH binaries}, i, t}}{N_{\text{sample}, i, t}} \cdot \frac{N_{\text{merger}, i, t}}{\Delta t}. \quad (21)$$

In Eq. (21), t_{look} is the look back time, for N_{shells} number of spherical shells that we divide the dark matter halo. Also, $N_{\text{sample}, i, t}$ is the number of PBH binaries that are sampled at the shell i at a given timestep associated with time t . $N_{\text{PBH binaries}, i, t}$, is the true number of PBH binaries in the shell i at time t . $N_{\text{merger}, i, t}$ is the number of the binaries that merged in our simulation within the mass shell i , at the timestep associated with time t . Our timesteps have a duration of Δt . For more details on the simulations see Ref. [31].

Additionally, to the above mentioned quantities, the initial distribution functions of the PBH binaries' orbital parameters a_0 (for the semi-major axis) and e_0 (for the eccentricity), depend on the PBH mass distribution. These initial distributions of the PBH binaries' properties, originate from the initial early universe conditions at the creation of PBHs. In our simulations, for each of our

binaries, we randomly pick its initial values of semi-major axis and eccentricity from these initial distribution functions. We then evolve a and e , based on Eqs. (4) and (5). In Appendix B, we provide further details on how we calculate the initial distribution functions of the PBH binaries' orbital properties for the continuous log-normal PBH mass distribution.

In Fig. 2, for log-normal distributions with $\sigma = 0.6$, we show the total merger rate as a function of m_c (red dashed line). A choice of $\sigma \ll 0.6$, would give a mass distribution effectively identical to a monochromatic one, given the current mass resolution capacity of LVK. Instead, values of $\sigma \gg 0.6$, will result in very wide mass distributions for the PBH binaries. Given the limited number of observed binaries by LVK, such a PBH component to the data is very difficult to separate from a more conventional power-law distribution in the masses of the black holes. The log-normal mass-distribution provides a relatively higher rate than the monochromatic one.

III. SIMULATING THE DETECTABILITY OF PRIMORDIAL BLACK HOLE BINARIES AND SETTING LIMITS

In order to set limits on a PBH component to the LVK O1-O3 observations, we implement the methodology of Ref. [33]. To simulate the LVK observations, we generate merging PBH binaries with masses m_1 and m_2 , following the relevant PBH mass-distribution (monochromatic or log-normal). These merging PBH binaries, have the redshift distribution $R_{\text{total}}(z)$ described earlier. For all these merging binaries we evaluate their signal-to-noise ratio (SNR) and retain the binaries with a $\text{SNR} > 8$. We also generate a population of ‘‘conventional’’ black hole binaries with m_1 following a power-law distribution: $dN/dm_1 \propto m_1^{-\alpha}$ and the ratio of the secondary mass over the primary mass $q = m_2/m_1$ following a power-law distribution as well, $dN/dq \propto q^\beta$. These binaries have a redshift distribution that resembles that of star formation [45]. Their comoving rate density is $dR/d(z+1) \propto (1+z)^\kappa$, with $\kappa = 2.9$. Our assumptions on this conventional population of black hole binaries follow the same prescription of studying the LVK observations as Ref. [46] (see also [12]). We refer to this population of black holes as a power-law population or just ‘‘PL’’. We retain the conventional PL population of black hole binaries with $\text{SNR} > 8$. We then compare the combined population of merging PBH binaries and black hole binaries from a PL population to the m_1 - and q -histograms of the LVK O1-O3 observations, presented in Ref. [33]. For a given choice of PBH mass distribution, we marginalize over the values of α , β and the normalizations of the PBH and PL components.

We consider 15 bins of redshift, with values from $z=0$ to $z=0.75$ in increments of 0.05. Above a redshift of 0.75 binaries are not detectable using the O3 noise curve provided by the LVK collaboration [47]. The number of

mergers in a bin with edges z_1 and z_2 is,

$$N_{\text{merger}}(z_1, z_2) = 4\pi \int_{z_1}^{z_2} \frac{c \cdot \chi(z)^2 \cdot R_{\text{total}}(z)}{(1+z)H(z)} dz, \quad (22)$$

with $\chi(z)$ the comoving distance, $R_{\text{total}}(z)$ the PBH comoving merger rate and $H(z)$ the Hubble expansion parameter.

In the LVK observations, there is a generic uncertainty on the derived masses of the detected black hole binaries. For a monochromatic PBH component, we approximate that error by convolving with a Gaussian that has a mass-dependent width (see table IV in [33] for further details). Thus, even for an underlying monochromatic PBH population, the generated PBH binaries have masses m_1 and m_2 with $m_2 \leq m_1$. For a given underlying m_{PBH} we draw the m_1 and m_2 masses from the relevant Gaussian density function, with a width dependent on m_{PBH} . For instance for $m_{\text{PBH}} = 10 M_\odot$, the Gaussian has a $\pm 1\sigma$ -width of $\pm 2.1 M_\odot$, while for $m_{\text{PBH}} = 30 M_\odot$, the $\pm 1\sigma = \pm 5.1 M_\odot$ (see Ref. [33] for more details). For the case of the log-normal PBH mass distribution, we first convolve the relevant underlying distribution with a Gaussian whose width depends on the value of the underlying PBH mass. A log-normal distribution predicts PBHs with a wide range of masses. A $10 M_\odot$ PBH will have its mass measured by LVK with a different uncertainty than a $60 M_\odot$ PBH. We account for that mass-dependency in our simulated events. We subsequently draw the m_1 and m_2 values from that final distribution.

In deriving the best-fit and the 95% upper limit normalization of the PBH component, for a given choice of PBH mass, we marginalize over the values of α , β describing the PL black hole binaries population. We perform a χ^2 fit of the combined PBH and PL populations to the the LVK m_1 - and q -histograms of Ref. [33].

The simulated $R_{\text{total}}(z)$ for the PBH population assumes $f_{\text{PBH}} = 1$ and $f_{\text{PBH binaries}} = 0.5$, that once fitting to the data gets significantly suppressed. The normalization factor of the PBH population is proportional to f_{PBH}^2 , but scales in a less trivial manner with $f_{\text{PBH binaries}}$, relevant for the PBH merges induced by binary-single interactions.

It is important to note that due to the small LVK detected merger events, our current statistical errors are quite large. In addition, LIGO's O3 noise curves are time dependent, a piece of information not directly accessible to us. We used the noise curves of Ref. [47], for the entire observing run time.

The total merger rate's R_{total} relation to f_{PBH} and $f_{\text{PBH binaries}}$ is,

$$R_{\text{total}} = f_{\text{PBH}}^2 (R_{\text{captures}} + 2 \cdot f_{\text{PBH binaries}} \cdot R_{\text{binary-single}}), \quad (23)$$

where the factor of 2 is because the $R_{\text{binary-single}}$ component is evaluated for $f_{\text{PBH binaries}} = 0.5$.

Fitting the amplitude of the PBH component (i.e. its total comoving rate) to the LVK observations we directly

probe f_{PBH}^2 , which we refer to as $f_{\text{PBH, LVK}}^2$. For any value of $f_{\text{PBH binaries}}$, we get for f_{PBH} ,

$$f_{\text{PBH}} = \left(\frac{f_{\text{PBH, LVK}}^2 \cdot R_{\text{total}}}{R_{\text{captures}} + 2 \cdot f_{\text{PBH binaries}} \cdot R_{\text{binary-single}}} \right)^{1/2}. \quad (24)$$

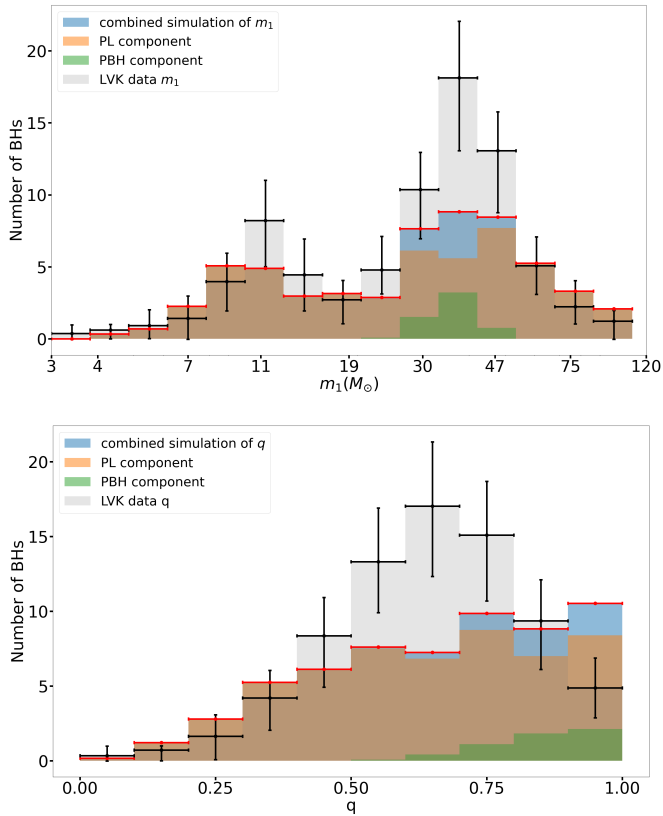


FIG. 3. Normalized m_1 -histogram (top) and q -histogram (bottom) of the simulated (in blue) and detected by LVK (in gray) black hole binaries with a $\text{SNR} > 8$. The simulated binaries are a combination of a dominant PL population (in brown) and a population of PBH binaries (in green). See text for further details.

In Fig. 3, we give the m_1 -histogram (top panel) and the q -histogram (bottom panel) of simulated black hole binaries detectable with a $\text{SNR} > 8$ at O3 run sensitivity. The underlying simulation includes the PL populations with $\alpha = 3.44$ and $\beta = -1$. The PBH component is for $m_{\text{PBH}} = 35 M_\odot$, with $f_{\text{PBH}} = 1.44 \times 10^{-2}$. Superposed to that, is the m_1 -histogram of the LVK observed black hole binaries with Poisson error-bars (see Ref. [33]). The normalizations of the two populations and the values of α and β are chosen in order for their sum to provide a best fit to the *combined* m_1 - and q -histograms. Since a prominent PBH population, would result in many binaries with $q \simeq 1$, which is not supported by the LVK observations the normalization of the PBH component is smaller than what would have been derived using only the m_1 -histogram. We provide examples of m_1 - and q -histograms for the monochromatic PBH population for

increased values of f_{PBH} , along with an example of best fit results for a PBH population following a log-normal distribution in Appendix C.

The 95% upper limits are obtained by first fitting the LVK histograms with a PL population of black hole binaries, without a PBH component. That gives a best fit χ^2 of 33.46, for $\alpha = 3.44$ and $\beta = -1$. Then to get an upper limit on the PBH population we find the maximum normalization to the PBH component for which we get a $\chi^2 = 33.44 + 2.71 = 36.15$.

We obtain two sets of values for f_{PBH} and $f_{\text{PBH binaries}}$. One set is for the best fit χ^2 PBH normalization, and the other is the 95% upper limit on f_{PBH} . In Table I, we give these values of f_{PBH} , fixing $f_{\text{PBH binaries}} = 0.5$. In that table, our second and third columns give our results for the monochromatic case, while the fourth and fifth the log-normal distribution.

m_{PBH} (M_\odot)	$f_{\text{PBH, mon.}}^{\text{best-fit}}$ ($\times 10^{-2}$)	$f_{\text{PBH, mon.}}^{95\% \text{ upper}}$ ($\times 10^{-2}$)	$f_{\text{PBH, log-n.}}^{\text{best-fit}}$ ($\times 10^{-2}$)	$f_{\text{PBH, log-n.}}^{95\% \text{ upper}}$ ($\times 10^{-2}$)
5	3.6	10	3.4	8.5
10	0	7.9	3.2	5.9
15	0	5.2	1.9	3.7
20	2.9	5.8	1.2	2.7
25	1.8	3.2	0.70	2.1
30	1.4	2.5	0	1.7
35	1.4	2.3	0	1.5
40	1.2	2.0	0	1.3
45	0.77	1.6	0	1.2
50	0.64	1.5	0	1.1
60	0	0.88	0	0.96
80	0	0.55	0	0.85

TABLE I. Obtained values on f_{PBH} for $f_{\text{PBH binaries}} = 0.5$. First column gives the mass of a monochromatic PBH population with mass m_{PBH} , or the value of m_c for a log-normal distribution. Second and third columns give the f_{PBH} , best-fit ($f_{\text{PBH, mon.}}^{\text{best-fit}}$) and 95% upper limit value ($f_{\text{PBH, mon.}}^{95\% \text{ upper}}$) respectively, for an underlying monochromatic PBH mass-distribution. Similarly, the fourth and fifth columns give the f_{PBH} , best-fit ($f_{\text{PBH, log-n.}}^{\text{best-fit}}$) and 95% upper limit ($f_{\text{PBH, log-n.}}^{95\% \text{ upper}}$) respectively, for an underlying log-normal PBH mass-distribution. For the case where a PBH component provides a better fit to the PL only population of black hole binaries, we get $f_{\text{PBH}}^{\text{best-fit}} > 0$ (second or fourth column).

The LVK m_1 -histogram shown (in light gray) in Fig. 3 has two peaks. One approximately at $12 M_\odot$ and the other at $35 M_\odot$. We obtain best-fit values for a PBH component with m_{PBH} around the second peak (see Table I, second column). However, for $m_{\text{PBH}} = 10 M_\odot$ and $15 M_\odot$ we get $f_{\text{PBH, best-fit}} = 0$. While a PBH component at $10 M_\odot$ or $15 M_\odot$ improves the m_1 -histogram's fit around the first peak, it also decreases the normalization of the PL population and its contribution to the LVK data in all other bins, including the second peak around $35 M_\odot$. This leads to a worse fit overall. On the other hand, for the log-normal PBH distribution we get a preference for PBH component only for $m_c < 30 M_\odot$.

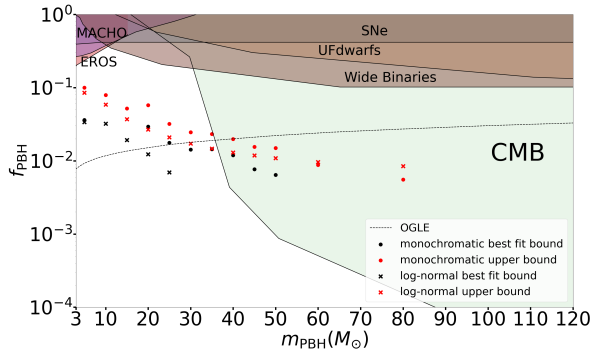


FIG. 4. Our results on f_{PBH} as a function PBH mass, assuming $f_{\text{PBH binaries}}=0.5$. Dots are for a monochromatic distribution, while “x” symbols for a log-normal distribution where $m_{\text{PBH}} = m_c = e^\mu$ of Eq. (14). Blue symbols represent best fit values for f_{PBH} , i.e. there is statistical preference for a PBH contribution to the LVK observations. Red symbols are for the 95% upper limits on f_{PBH} . We also provide for comparison upper limits from other probes on PBHs. See text for more details.

In Fig. 4, we plot our results on f_{PBH} for a monochromatic distribution of PBHs (dots) as well as a log-normal distribution of PBHs (“x” symbols). This figure includes both the values of f_{PBH} associated to the best fit to the LVK data (blue dots and “x”) and the 95% upper limits on f_{PBH} (red dots and “x”). In addition we show already established limits from Refs. [48–55] (limits obtained from [56, 57]).

Fig. 5, shows the difference in the χ^2 fit values of a PL + PBH population and a PL population of black holes only. As explained earlier, for the PL only population we get a best fit of $\chi^2 = 33.44$. When we study the PL+PBH case for a given value of f_{PBH} in each case we marginalize over the properties of the PL population (values of power-laws α , β and overall normalization). We also fix here $f_{\text{PBH binaries}} = 0.5$. We show our results for the same 12 masses of Table I. White regions are for a $\Delta\chi^2 = 0$, i.e. $\chi^2 = 33.44$. Blue regions are for $\Delta\chi^2 < 0$, measuring the improvement in the χ^2 -value by having a PBH population. Instead, the red regions for $\Delta\chi^2 > 0$ are used to set upper limits on the PBH population’s amplitude. We assume a monochromatic PBH population for the top panel and for the bottom panel a log-normal PBH mass-distribution with $\mu = \ln(m_c)$ and $\sigma = 0.6$.

For masses of $30 - 40 M_\odot$ there is a small improvement on the χ^2 value, by $\Delta\chi^2 \simeq 2$, compared to the best-fit PL population only case. This better fit is for $f_{\text{PBH}} \simeq 1 - 2 \times 10^{-2}$ (see Fig. 5). The 95%, 99.5% and 99.87% upper limits on f_{PBH} , are also represented in Fig. 5. They are associated with a $\Delta\chi^2$ of 2.71, 6.63 and 9.00 respectively.

In Fig. 6, we present the 95% upper limits on f_{PBH} as a function of the monochromatic PBH mass m_{PBH} , for different choices of $f_{\text{PBH binaries}}$ (top panel). As we explore a range of values for $f_{\text{PBH binaries}}$ of 0.1, 0.5, 0.7 and 1 respectively, we observe that the enhancement in $f_{\text{PBH binaries}}$ suppresses f_{PBH} . This is due to the dom-

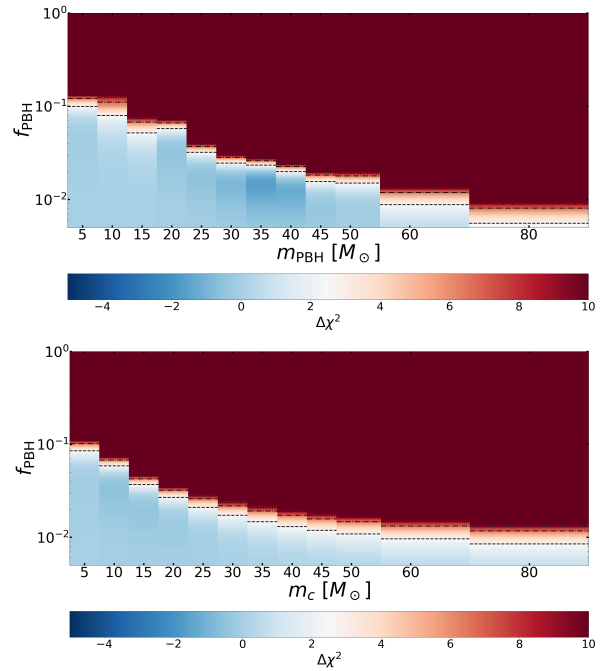


FIG. 5. We present here the χ^2 fit for different choices of f_{PBH} at different masses for the monochromatic (top plot) and the log-normal (bottom plot) PBH distribution. The color gradient indicates the difference between the χ^2 values using a power-law + PBH component and the best fit χ^2 value of the power-law component only. The black dashed, dotted-dashed and dotted lines give the region of parameter space that is within 95%, 99.5% and 99.87% upper limits respectively. See text for further details.

inant contribution of PBH binary-single interactions to the total PBH merger rate. The calculation is performed at redshift $z = 0$ using Eq.(24), with the upper limits on f_{PBH} presented in Table I for $f_{\text{PBH binaries}} = 0.5$. Moreover, at the bottom panel of Fig. 6, we show the 95% upper limits on $f_{\text{PBH binaries}}$ as a function of m_{PBH} and how possible choices of f_{PBH} affects it. We observe a similar behavior as $f_{\text{PBH binaries}}$ is being suppressed by enhancing f_{PBH} . We show results for f_{PBH} of 0.02, 0.04, 0.06 and 0.1.

For the log-normal PBH mass-distribution, we find similar limits on f_{PBH} to those derived for the monochromatic case. This is shown in Fig. 4, (compare dots with “x’s”) and in the results of Table I. One distinction between the results for the monochromatic and the log-normal distributions, is that the mass range for which we get a (small statistical) preference for a PBH component is moved at lower masses for the log-normal assumption.

The selection of simulated events with $\text{SNR} > 8$ changes significantly the shape of the original distribution. In Fig. 7, we plot the normalized PBH mass distribution, i.e. probability density function (PDF). Our blue histogram is the true underlying log-normal distribution for $m_c = 15 M_\odot$, giving a peak of that distribution around the same value of mass. Our orange histogram

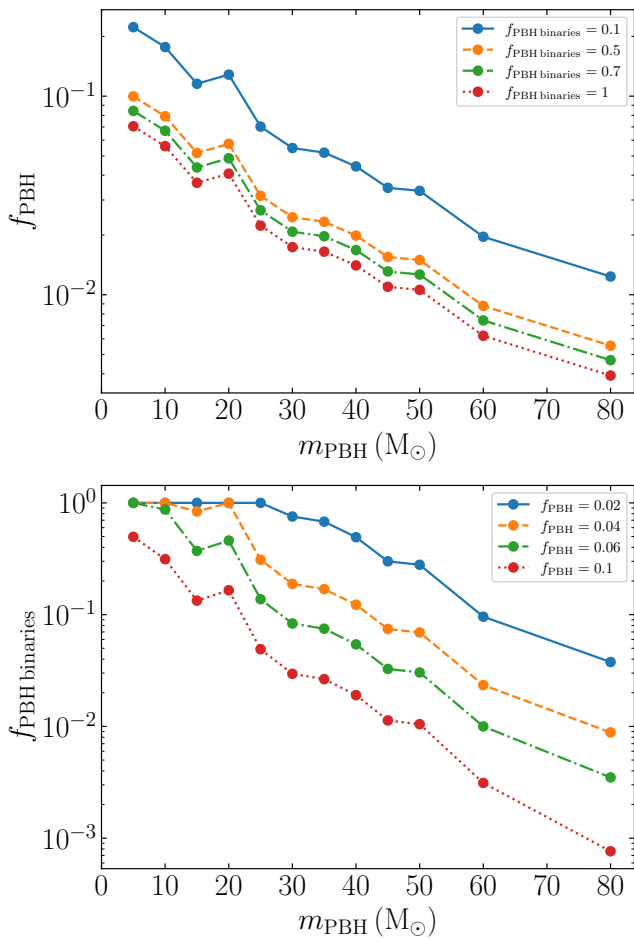


FIG. 6. *Top panel:* for the monochromatic PBH mass-distribution, we show how the 95% upper bound on f_{PBH} changes with m_{PBH} . We evaluate these limits by fixing $f_{\text{PBH binarities}}$ to $(0.1, 0.3, 0.7, 1)$. *Bottom panel:* the 95% upper limits on $f_{\text{PBH binarities}}$ as a function of m_{PBH} , fixing for each line f_{PBH} to $(0.02, 0.04, 0.06, 0.1)$.

give the PDF after convolving the original log-normal distribution with the Gaussian of mass-dependent width to account for the mass resolution of LVK. Finally, the green histogram shows the PDF on m_1 after retaining only the PBH binaries with a $\text{SNR} > 8$. The peak of the final observable population is shifted to a value of $35M_\odot$. From the χ^2 map of Fig. 5, derived for the log-normal mass-distribution (bottom panel), we see that such a distribution with a peak near $m_c = 15M_\odot$ is better than a power-law fit alone. This is due to the effect of selecting binaries with a $\text{SNR} > 8$, which shifts the peak closer $40M_\odot$ (see figure 7), around which there is a significant peak present in the LVK m_1 -histogram.

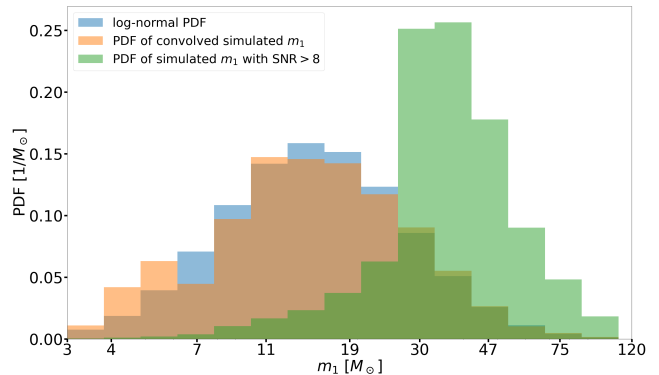


FIG. 7. Histograms showing the PDFs of the mass of PBHs with a log-normal mass distribution with a peak at $15M_\odot$ and $\sigma = 0.6$ (in blue), the convolved log-normal PDF with Gaussians to take into account the uncertainty on the derived masses (in orange). In green we show the PDF of the events simulated to have a $\text{SNR} > 8$, drawn from the log-normal distribution that is convolved with the Gaussians (i.e. the orange PDF).

IV. DISCUSSION AND CONCLUSIONS

In this paper we have explored the impact of the recent LVK observing runs (O1-O3) on the abundance of PBHs. We present limits for monochromatic PBHs and for PBHs following a log-normal mass-distribution. Given the limited mass resolution of the LVK observations, for the log-normal distribution, we choose a width that can be distinguished from the monochromatic case, while also would not be confused to being part of a population of black hole binaries that would roughly follow a power-law distribution in their mass.

We evaluate the rates of PBH mergers including both binaries formed in direct captures due to the GW emission from very close encounters in dark matter halos and merges of PBH binaries with orbital properties evolving via their interaction with other near-by PBHs, that are either single PBHs or in loose binaries within such halos. For the monochromatic case, we use directly the simulated results of Ref. [31], that evaluated the rates of PBHs at $m_{\text{PBH}} = 30M_\odot$ inside halos of masses $10^3 - 10^{15}M_\odot$, implementing those simulations to the relevant mass range of $5-80M_\odot$ that can be constrained by the current LVK observations (see discussion in Sec. II A). For the log-normal PBH mass-distribution we have implemented a similar set of simulations as described in Sec. II B. Irrespective of the exact mass assumptions, PBH binaries whose orbital properties evolve via interactions with other PBHs inside halos, can significantly enhance the total PBH merger rate compared to the merging binaries formed from direct captures. Our simulations of the PBH binaries interacting with other near-by PBHs account for both the distribution of the orbital properties (semi-major axis and eccentricity distributions) and for the relevant environmental factors (density

of objects, relative velocities and interacting masses). In our simulations the dark matter halos' properties within which these interactions take place are fully evolved from redshift of 12 to our present time (see discussion in Sec. II and Ref. [31]). We present the total merger rates of PBHs from either a monochromatic or a log-normal mass distribution at redshift of zero in Fig. 2, for different mass-choices. Given that these rates represent the most minimal PBH merger rates taking place inside dark matter halos our limits are robust and conservative.

We derive our limits by analyzing the VLK binary black hole primary mass m_1 and mass-ratio q distributions. We focus on the 72 merger events detected by LVK during the observing runs O1-O3 with a secondary mass $m_2 \geq 4 M_\odot$ and with a false alarm rate of FAR $< 1 \text{ yr}^{-1}$. Following Ref. [33], we can use histograms of the m_1 - and q -distributions, as those shown in Figs. 3, 9, 10 and 11. The observed black hole binaries are modeled to be the sum of two distinct populations of binaries. Most black hole binaries are assumed to have their m_1 , q and co-moving rate density distribution properties described by simple power laws. We refer to that population as PL population of binaries (see discussion in Sec. III also Refs. [33, 46]). The second population is merging PBH binaries. Such an analysis of the LVK observations allows for a rapid search of the range potentially describing the underlying binary black hole population.

Our limits presented in Figs. 4 and 5 and in Table I, constrain the dark matter abundance in PBHs to a fraction by mass of $10^{-2} < f_{\text{PBH}} < 10^{-1}$. These limits derived directly from the GW observations, probe directly the existence of PBHs in the late stages of the universe and thus provide one of the most robust and direct ways to search for them. In addition, we get some of the tightest limits in the literature on the abundance of PBHs with mass in the range of 3-40 M_\odot (see also [58]).

As the dominant contribution to the PBH merger rate comes from the hardening of existing PBH binaries when interacting with other PBHs, our limits depend on the assumed fraction of PBHs in binaries $f_{\text{PBH binaries}}$, at their creation in the early universe (before the formation of dark matter halos). For this reason we allow for a range of options on that fraction; showing in Fig. 6 how varying that parameter affects our limits (see also discussion in Sec. III).

With upcoming results from the LVK fourth run and future final design sensitivity run, we expect the total number of black hole binaries to increase by nearly a factor of ten. That improvement alone, will allow us to derive limits on the abundance of PBHs that is going to be at least a factor of three tighter. That is if the second peak in the LVK data (around masses of $m_1 = 35 M_\odot$), is simply a selection effect due to the LVK interferometers' sensitivity and not a true feature of the underlying black hole binaries' population. Even with the current very low statistics of the LVK observations, we find a minor statistical preference for a population of PBHs with masses $\sim 30 M_\odot$ (for a monochromatic case) for $f_{\text{PBH}} \simeq 10^{-2}$

(see Fig. 5). Moreover, the future observations by LVK will allow us to probe for black holes with masses $< 4 M_\odot$, i.e. in the low-mass gap, a parameter range conventionally though devoid of regular stellar origin black holes. With future observations one may also be able to include information on the effective spins of the detected binaries. We leave such a possibility for future work.

We have made publicly available our results for the PBH merger rates and for the derived PBH limits through Zenodo in <https://zenodo.org/records/14768441>. Additionally, the LVK m_1 - and q -histograms used to derive the PBH limits in this work are in <https://zenodo.org/records/14675445> (associated to Ref. [33]).

ACKNOWLEDGMENTS

The authors would like to thank David Garfinkle and Jason Krommydas for valuable discussions. MEB, MA and IC are supported by the National Science Foundation, under grant PHY-2207912.

Appendix A: Hard PBH binaries inside dark matter halos

As described in the main text, only the hard PBH binaries with $a \leq a_h$ will harden (become dynamically tighter) via binary-single interactions and can merge within a Hubble time. The fraction of all PBH binaries that are hard depends on their environments, as in Eq. (10), a_h depends on the dispersion velocity $v_{\text{disp}}(r, t)$ of surrounding PBH objects. In this appendix we show results on how exactly the various dark matter halo environments affect the fraction of hard PBH binaries f_{hard} .

In massive dark matter halos, the dispersion velocity $v_{\text{disp}}(r, t)$ is high. This means that there is a smaller fraction of hard binaries f_{hard} , compared to smaller halos, where the velocity dispersions are lower. In fact in the smallest halos that we study, all PBH binaries are hard. Furthermore, the fraction of hard binaries in an evolving halo also changes with time. As the dark matter halos grow in mass, early in the halo's evolution, there is a larger fraction of hard binaries, leading to higher merger rates. This evolution of f_{hard} is most prominent in halos that grow to be massive by $z = 0$. In the halos that have low mass at $z = 0$, almost all binaries are hard, throughout the simulation time.

Different choices on the value of the monochromatic PBH mass, m_{PBH} , affect our results as well. A larger value of m_{PBH} , leads to a larger value on a_h , which in turn increases the fraction of hard binaries and their merger rate due to binary single interactions. We remind the reader that the two-body capture rate does not depend on the PBH mass. However, it does depend on v_{disp} , with increasing rates at high redshifts. A full analysis of these effects has been recently done in Ref. [31].

Halo Mass (M_\odot)	Shell Index	a_h (au)	f_{hard} (%)
10^3	-	4.48×10^5	100.
10^6	1	2.08×10^{-1}	99.6
10^6	3	1.79×10^{-2}	41
10^6	5	3.17×10^{-2}	61
10^9	1	7.07×10^{-2}	87
10^9	6	4.20×10^{-4}	0.67
10^9	10	3.17×10^{-4}	0.46
10^{12}	1	1.07×10^{-2}	27
10^{12}	6	1.79×10^{-5}	0.022
10^{12}	10	3.17×10^{-6}	0.003
10^{15}	1	2.26×10^{-3}	5.1
10^{15}	6	1.21×10^{-6}	0
10^{15}	10	3.17×10^{-8}	0

TABLE II. For a range of dark matter halo masses (first column) and at different radial distances (second column) from the center of the halos, we provide in the last column the fraction of hard binaries, f_{hard} (in %). We give results at $z = 0$. We sampled $N = 10^5$ binaries in each halo. We used the case of a monochromatic $30 M_\odot$ PBHs. For reference we also provide the value of a_h for the given environment (second to last column).

In Table II, we provide the derived f_{hard} at $z = 0$, for a range of halo masses (first column). For the most massive halos there is a gradient on the value of $v_{\text{disp}}(r, t)$ as one moves away from the center of the halo, which affects the value of a_h (third column) and f_{hard} (fourth column).

In these calculations, for the dark matter halos with mass of $10^3 M_\odot$ we assumed a uniform density evaluated from the NFW profile at $R_{\text{vir}}/2$. For the smallest halos there is no radial gradient on the velocity dispersion, as a PBH's crossing time through the halo is too small compared to the evolution timescale. For $10^6 M_\odot$ halos we used five radial shells, while for the more massive $10^{12} M_\odot$ and $10^{15} M_\odot$ halos, ten radial shells. The shell index starts at one for the innermost shell and increases outward. For more details on the structure of the simulations see Ref. [31].

Appendix B: The orbital properties of PBH binaries before halo formation

Since our goal is to simulate the evolution and merger rates of PBH binaries, we need to know the initial value of their orbital properties (a_0, e_0). In this appendix, we provide the initial distribution of (a_0, e_0), of PBH binaries at their formation. For the case of PBH binaries with monochromatic mass, a detailed discussion about the distribution of their orbital parameters is given in [32, 59–61]. We follow the exact assumptions outlined in [61] (see also Ref. [31]), to calculate the the initial distribution of (a_0, e_0) of PBH binaries. In this work, we also simulate the merger rates of PBH binaries following a log-normal mass distribution. For such binaries the distribution of their orbital properties depends on their

mass distribution at formation. Thus, we need to modify the formulation and assumptions provided in [61] and extend it to the case of a log-normal distribution. We simply take expectation values for terms that include the PBH's mass.

The mean separation between an initial pair of PBHs is,

$$\bar{x} = \left(\frac{3(m_{\text{PBH},1} + m_{\text{PBH},2})}{8\pi f_{\text{PBH}} \rho_{\text{eq}}} \right)^{1/3}, \quad (\text{B1})$$

where ρ_{eq} is the average energy density in the matter-radiation equality (at $z \simeq 3450$) and $m_{\text{PBH},1}$ and $m_{\text{PBH},2}$ are the masses of the two PBHs forming the binary.

The distribution of the semi-major axis depends on \bar{x} and the rescaled angular momentum $j \equiv \sqrt{1 - e^2}$ that read as follows,

$$P(j) = \frac{y(j)^2}{j(1 + y(j)^2)^{3/2}} \quad \text{and} \quad (\text{B2})$$

$$y(j) = \frac{j}{0.5(1 + \sigma_{\text{eq}}^2/f_{\text{PBH}}^2)^{1/2}(x/\bar{x})^3}. \quad (\text{B3})$$

The parameter $\sigma_{\text{eq}} \approx 0.005$, is the variance of the Gaussian large-scale density fluctuations during matter-radiation equality. This distribution is the sum of the effect by torques from nearby PBHs and matter perturbations during the PBH binary's formation [60]. Ultimately, the distribution that characterizes both j and the semi-major axis a can be expressed as,

$$P(a, j) = \frac{3 \cdot a^{-1/4}}{4} \left(\frac{f_{\text{PBH}}}{\zeta \bar{x}} \right)^{3/4} P(j) \exp \left[- \left(\frac{x(a)}{\bar{x}} \right)^3 \right], \quad (\text{B4})$$

with

$$x(a) = \left(\frac{3a(m_{\text{PBH},1} + m_{\text{PBH},2})}{8\pi \zeta \rho_{\text{eq}}} \right)^{1/4} \quad (\text{B5})$$

and $\zeta = 0.1$ [32].

The parameters \bar{x} and $x(a)$, can therefore be calculated for any given pair of ($m_{\text{PBH},1}, m_{\text{PBH},2}$). However, as described in the main text, when PBHs follow a log-normal mass-distribution with the function $\psi(m)$ of Eq. (14), the values for ($m_{\text{PBH},1}, m_{\text{PBH},2}$) span a range. To account for such a range, we evaluate \bar{x} and $x(a)$ analytically by integrating over the respective mass distribution functions $\psi(m_1)$ and $\psi(m_2)$ as,

$$\langle \bar{x} \rangle = \int_{m_{1\text{min}}}^{m_{1\text{max}}} dm_1 \int_{m_{2\text{min}}}^{m_{2\text{max}}} dm_2 \psi(m_1) \psi(m_2) \times \left(\frac{3(m_1 + m_2)}{8\pi f_{\text{PBH}} \rho_{\text{eq}}} \right)^{1/3}. \quad (\text{B6})$$

and

$$\langle x(a) \rangle = \int_{m_{1\text{min}}}^{m_{1\text{max}}} dm_1 \int_{m_{2\text{min}}}^{m_{2\text{max}}} dm_2 \psi(m_1) \psi(m_2) \times \left(\frac{3a(m_1 + m_2)}{8\pi \zeta \rho_{\text{eq}}} \right)^{1/4}. \quad (\text{B7})$$

With, m_1 and m_2 the $m_{\text{PBH},1}$ and $m_{\text{PBH},2}$ respectively.

In Fig. 8, we show in the green-lined histogram the semi-major axis distribution for the PBH binaries at their initial conditions. We assumed a log-normal mass distribution with $\mu = \ln(30)$ and $\sigma = 0.6$. We also show for comparison, in the red-lined histogram the equivalent semi-major axis distribution for binaries made out of monochromatic $m_{\text{PBH}} = 30M_\odot$ PBHs. We simulated 10^5 PBH binaries.

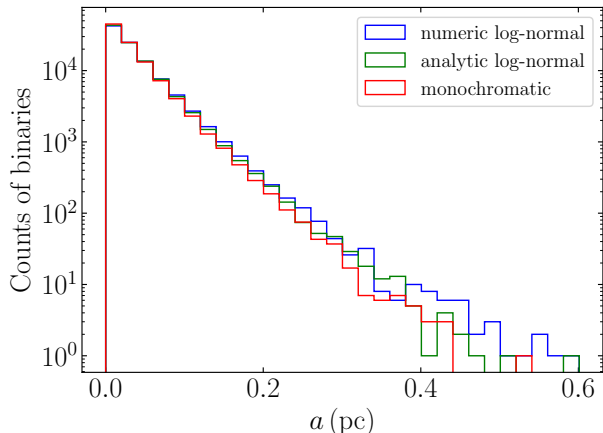


FIG. 8. The initial semi-major axis of PBHs, calculated for monochromatic PBHs with $m_{\text{PBH}} = 30M_\odot$ (red line) and for a log-normal distribution with $\mu = \ln(30)$ and $\sigma = 0.6$. For the log-normal distribution we present results through two different prescriptions; a fully numerical Monte Carlo simulation “numeric” (shown by the blue line) and an analytical prescription (green line). See text for more details.

While Eqs. (B6) and (B7), provide an analytical prescription to get the PBH binaries’ semi-major axis distribution, we have also run a Monte Carlo simulation of these binaries’ distribution (shown by the blue-line “numeric log-normal” histogram). For the numeric-log-normal prescription, we generated the masses (not taking the mean of the mass terms), $m_{\text{PBH},1}$ and $m_{\text{PBH},2}$ in the expression for \bar{x} and $x(a)$ given by Eqs. (B1) and (B5). We applied the inverse transform sampling method to the log-normal distribution. This calculation lead to the generation of unique values for \bar{x} and $x(a)$ (though very similar values) for each binary we sampled. This means that, unlike the analytical prescription, we calculated the separation between each binary we sampled and did not assume one mean separation \bar{x} for all binaries as in the case of the analytical log-normal. The difference between the numerical and the analytical prescriptions on the resulting distributions of the semi-major axes of the PBH binaries at creation, are minute.

Appendix C: Examples of m_1 and q histograms from our fits to the LVK data

In Fig. 3, we presented the fitted m_1 - and q -histograms associated to a combination of a PL and PBH component (using $m_{\text{PBH}} = 35M_\odot$ as an example). While adding a PBH component improves the fit to the m_1 -histogram alone, for masses around its second peak, we noticed that the quality of the fit to the q -histogram is always poorer compared to a PL component only. For the example of Fig. 3, its bottom panel, we get a χ^2 fit to the LVK q -histogram of $\chi^2_{\text{PL} \& \text{PBH},q} = 19.7$. By comparison fitting the q -histogram by a simple PL component we get $\chi^2_{\text{PL},q} = 17.8$.

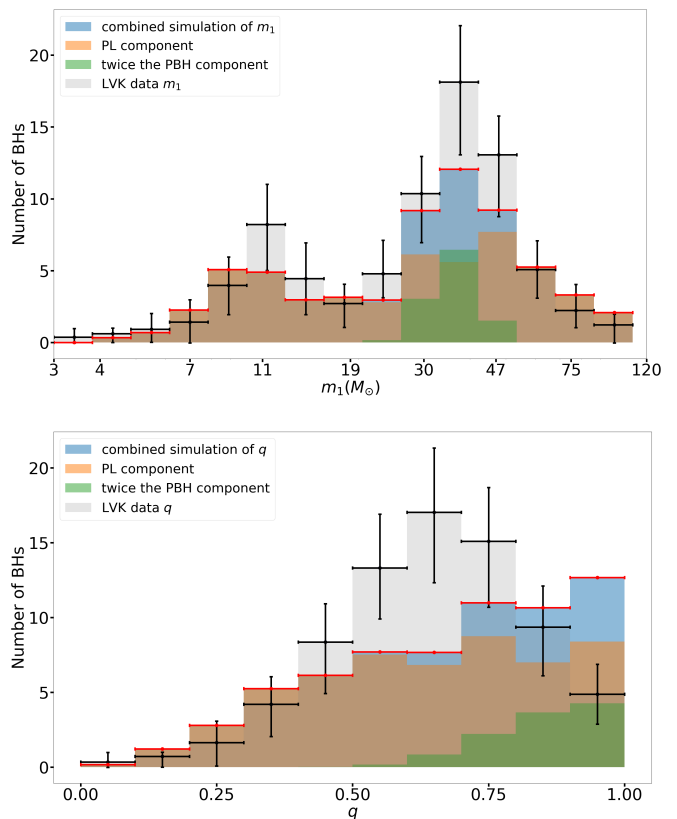


FIG. 9. As in Fig. 3, we show the normalized m_1 -histogram (top) and q -histogram (bottom) of the simulated (in blue) and detected by LVK (in gray) black hole binaries with a $\text{SNR} > 8$. The simulated binaries are a combination of a dominant PL population (in brown) and double the best fit population of PBH binaries of Fig. 3 (in green). See text for further details.

A larger PBH component would lead to a better fit of the m_1 -histogram. However, the detrimental effect of the PBH component on the fitting of q , limits its normalization significantly. In Fig. 9 and Fig. 10 we present the m_1 - and q -histograms, using respectively double and triple the best-fit normalization to the PBH component of Fig. 3. The best-fit for a PL & PBH component gave $\chi^2_{\text{PL} \& \text{PBH best-fit}, m_1} = 12.2$ and $\chi^2_{\text{PL} \& \text{PBH best-fit}, q} =$

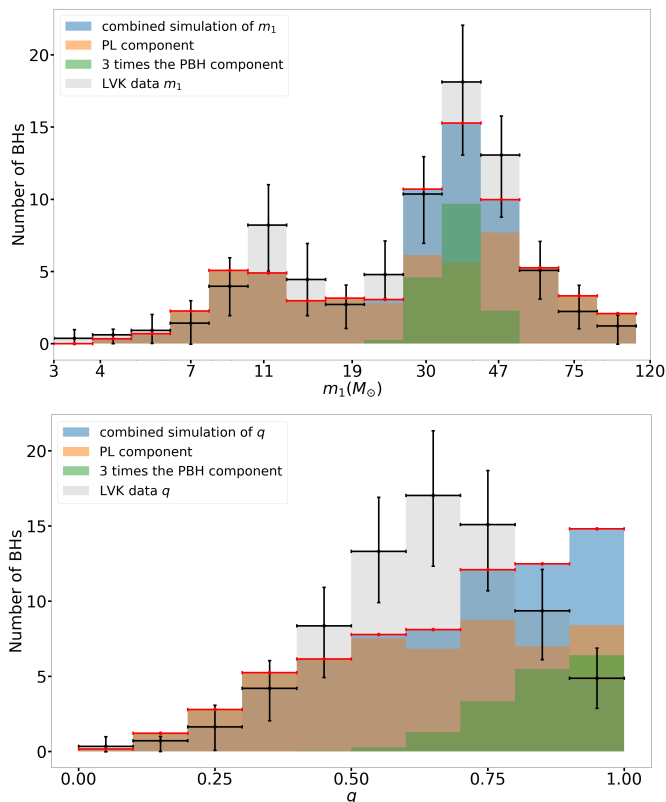


FIG. 10. As in Fig. 9, but instead using three times the (best fit) normalization for the PBH component that is shown in Fig. 3.

19.7, for $m_{\text{PBH}} = 35 M_{\odot}$ and $f_{\text{PBH}} = 1.44 \times 10^{-2}$. For the same $m_{\text{PBH}} = 35 M_{\odot}$, doubling f_{PBH} to 2.88×10^{-2} we get, $\chi_{\text{PL} \& 2 \times \text{PBH}, m_1}^2 = 8.5$ and $\chi_{\text{PL} \& 2 \times \text{PBH}, q}^2 = 25.87$. If we triple the f_{PBH} to 4.32×10^{-2} we get and $\chi_{\text{PL} \& 2 \times \text{PBH}, m_1}^2 = 6.43$ and $\chi_{\text{PL} \& 2 \times \text{PBH}, q}^2 = 35.27$. This shows that how a poor fit of the q -histogram of the LVK observations makes our limits on f_{PBH} significantly more restrictive.

Finally, in Fig. 11, we show the best fit assumptions for a PL and PBH population, where the PBHs follow a log-normal distribution with $\mu = \ln(15)$ and $\sigma = 0.6$. The best fit normalization is achieved for $f_{\text{PBH}} = 1.9 \times 10^{-2}$ (with $f_{\text{PBH binaries}} = 0.5$).

-
- [1] Marco Battaglieri *et al.*, “US Cosmic Visions: New Ideas in Dark Matter 2017: Community Report,” in *U.S. Cosmic Visions: New Ideas in Dark Matter (2017)* arXiv:1707.04591 [hep-ph].
- [2] Kimberly K. Boddy *et al.*, “Snowmass2021 theory frontier white paper: Astrophysical and cosmological probes of dark matter,” *JHEAp* **35**, 112–138 (2022), arXiv:2203.06380 [hep-ph].
- [3] B. J. Carr and S. W. Hawking, “Black holes in the early Universe,” *MNRAS* **168**, 399–416 (1974).
- [4] P. Meszaros, “The behaviour of point masses in an expanding cosmological substratum.” *Astronomy and Astrophysics* **37**, 225–228 (1974).
- [5] B. J. Carr, “The primordial black hole mass spectrum.” *Astrophys. J.* **201**, 1–19 (1975).
- [6] Simeon Bird, Ilias Cholis, Julian B. Muñoz, Yacine Ali-Haïmoud, Marc Kamionkowski, Ely D. Kovetz, Alvise Raccanelli, and Adam G. Riess, “Did LIGO detect dark matter?” *Phys. Rev. Lett.* **116**, 201301 (2016), arXiv:1603.00464 [astro-ph.CO].
- [7] Misao Sasaki, Teruaki Suyama, Takahiro Tanaka, and Shuichiro Yokoyama, “Primordial Black Hole Scenario for the Gravitational-Wave Event GW150914,” *Phys. Rev. Lett.* **117**, 061101 (2016), [Erratum: *Phys.Rev.Lett.* 121, 059901 (2018)], arXiv:1603.08338 [astro-ph.CO].
- [8] Sebastien Clesse and Juan García-Bellido, “The clustering of massive Primordial Black Holes as Dark Matter: measuring their mass distribution with Advanced LIGO,” *Phys. Dark Univ.* **15**, 142–147 (2017), arXiv:1603.05234 [astro-ph.CO].
- [9] Gianfranco Bertone and Tim Tait, M. P., “A new era in the search for dark matter,” *Nature* **562**, 51–56 (2018), arXiv:1810.01668 [astro-ph.CO].
- [10] Misao Sasaki, Teruaki Suyama, Takahiro Tanaka, and Shuichiro Yokoyama, “Primordial black holes—perspectives in gravitational wave astronomy,” *Class. Quant. Grav.* **35**, 063001 (2018), arXiv:1801.05235 [astro-ph.CO].
- [11] Bernard Carr and Florian Kuhnel, “Primordial Black Holes as Dark Matter: Recent Developments,” *Ann. Rev. Nucl. Part. Sci.* **70**, 355–394 (2020), arXiv:2006.02838 [astro-ph.CO].
- [12] Ely D. Kovetz, Ilias Cholis, Patrick C. Breysse, and Marc Kamionkowski, “Black hole mass function from gravitational wave measurements,” *Phys. Rev. D* **95**, 103010 (2017), arXiv:1611.01157 [astro-ph.CO].
- [13] Andrew D. Gow, Christian T. Byrnes, Alex Hall, and John A. Peacock, “Primordial black hole merger rates: distributions for multiple LIGO observables,” *JCAP* **01**, 031 (2020), arXiv:1911.12685 [astro-ph.CO].
- [14] Ely D. Kovetz, “Probing Primordial-Black-Hole Dark Matter with Gravitational Waves,” *Phys. Rev. Lett.* **119**,

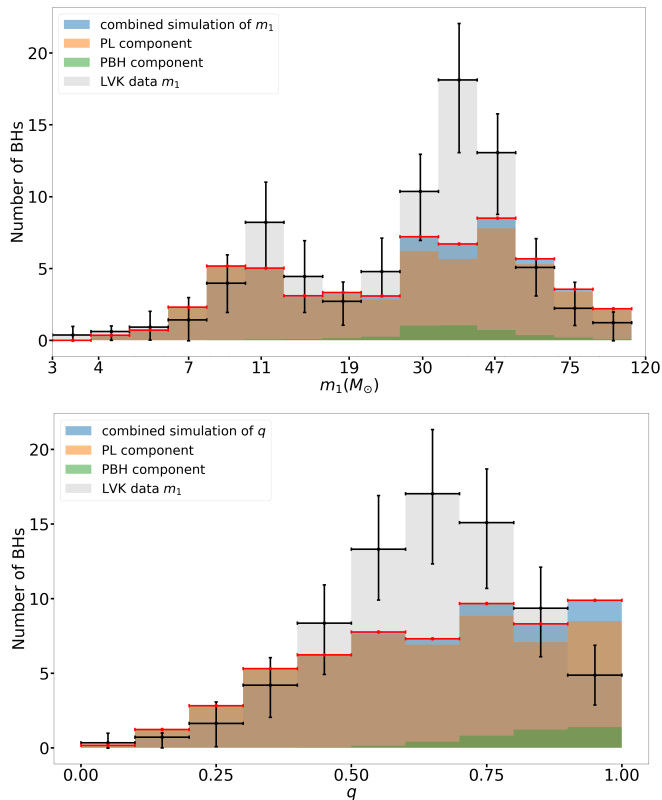


FIG. 11. As in Fig. 3, we show the normalized m_1 -histogram (top) and q -histogram (bottom) of the simulated (in blue) and detected by LVK (in gray) black hole binaries with a SNR > 8. The simulated binaries are a combination of a dominant PL population (in brown) and the best fit population generated from a log-normal distribution of PBHs

- 131301 (2017), arXiv:1705.09182 [astro-ph.CO].
- [15] Anuradha Gupta, Davide Gerosa, K. G. Arun, Emanuele Berti, Will M. Farr, and B. S. Sathyaprakash, “Black holes in the low mass gap: Implications for gravitational wave observations,” *Phys. Rev. D* **101**, 103036 (2020), arXiv:1909.05804 [gr-qc].
- [16] Jacob Golomb, Maximiliano Isi, and Will M. Farr, “Physical Models for the Astrophysical Population of Black Holes: Application to the Bump in the Mass Distribution of Gravitational-wave Sources,” *Astrophys. J.* **976**, 121 (2024), arXiv:2312.03973 [astro-ph.HE].
- [17] Alex Hall, Andrew D. Gow, and Christian T. Byrnes, “Bayesian analysis of LIGO-Virgo mergers: Primordial vs. astrophysical black hole populations,” *Phys. Rev. D* **102**, 123524 (2020), arXiv:2008.13704 [astro-ph.CO].
- [18] Zu-Cheng Chen and Alex Hall, “Confronting primordial black holes with LIGO-Virgo-KAGRA and the Einstein Telescope,” (2024), arXiv:2402.03934 [astro-ph.CO].
- [19] Irina Dvorkin, Jean-Philippe Uzan, Elisabeth Vangioni, and Joseph Silk, “Exploring stellar evolution with gravitational-wave observations,” *Mon. Not. Roy. Astron. Soc.* **479**, 121–129 (2018), arXiv:1709.09197 [astro-ph.HE].
- [20] Jordan Flitter, Julian B. Muñoz, and Ely D. Kovetz, “Outliers in the LIGO black hole mass function from coagulation in dense clusters,” *Mon. Not. Roy. Astron. Soc.* **507**, 743–760 (2021), arXiv:2008.10389 [astro-ph.HE].
- [21] Yuan-Zhu Wang, Shao-Peng Tang, Yun-Feng Liang, Ming-Zhe Han, Xiang Li, Zhi-Ping Jin, Yi-Zhong Fan, and Da-Ming Wei, “GW190521 and the GWTC-1 Events: Implication on the Black Hole Mass Function of Coalescing Binary Black Hole Systems,” (2020), arXiv:2009.03854 [astro-ph.HE].
- [22] Ilias Cholis, Konstantinos Kritos, and David Garfinkle, “Can Thorne-Żytkow objects source GW190814-type events?” *Phys. Rev. D* **105**, 123022 (2022), arXiv:2106.07662 [astro-ph.HE].
- [23] Ilias Cholis, “On the Gravitational Wave Background from Black Hole Binaries after the First LIGO Detections,” *JCAP* **06**, 037 (2017), arXiv:1609.03565 [astro-ph.HE].
- [24] Ilias Cholis, Ely D. Kovetz, Yacine Ali-Haïmoud, Simeon Bird, Marc Kamionkowski, Julian B. Muñoz, and Alvise Raccanelli, “Orbital eccentricities in primordial black hole binaries,” *Phys. Rev. D* **94**, 084013 (2016), arXiv:1606.07437 [astro-ph.HE].
- [25] Alvise Raccanelli, Ely D. Kovetz, Simeon Bird, Ilias Cholis, and Julian B. Muñoz, “Determining the progenitors of merging black-hole binaries,” *Phys. Rev. D* **94**, 023516 (2016), arXiv:1605.01405 [astro-ph.CO].
- [26] Vuk Mandic, Simeon Bird, and Ilias Cholis, “Stochastic Gravitational-Wave Background due to Primordial Binary Black Hole Mergers,” *Phys. Rev. Lett.* **117**, 201102 (2016), arXiv:1608.06699 [astro-ph.CO].
- [27] Davide Gerosa, Emanuele Berti, Richard O’Shaughnessy, Krzysztof Belczynski, Michael Kesden, Daniel Wysocki, and Wojciech Gladysz, “Spin orientations of merging black holes formed from the evolution of stellar binaries,” *Phys. Rev. D* **98**, 084036 (2018), arXiv:1808.02491 [astro-ph.HE].
- [28] Sebastien Clesse and Juan García-Bellido, “Detecting the gravitational wave background from primordial black hole dark matter,” *Phys. Dark Univ.* **18**, 105–114 (2017), arXiv:1610.08479 [astro-ph.CO].
- [29] Tomohiro Nakama, Joseph Silk, and Marc Kamionkowski, “Stochastic gravitational waves associated with the formation of primordial black holes,” *Phys. Rev. D* **95**, 043511 (2017), arXiv:1612.06264 [astro-ph.CO].
- [30] Gabriele Franciolini, Konstantinos Kritos, Emanuele Berti, and Joseph Silk, “Primordial black hole mergers from three-body interactions,” *Phys. Rev. D* **106**, 083529 (2022), arXiv:2205.15340 [astro-ph.CO].
- [31] Muhsin Aljaf and Ilias Cholis, “Simulating Binary Primordial Black Hole Mergers in Dark Matter Halos,” (2024), arXiv:2408.06515 [astro-ph.GA].
- [32] Yacine Ali-Haïmoud, Ely D. Kovetz, and Marc Kamionkowski, “Merger rate of primordial black-hole binaries,” *Phys. Rev. D* **96**, 123523 (2017), arXiv:1709.06576 [astro-ph.CO].
- [33] Mehdi El Bouhaddouti and Ilias Cholis, “On the mass distribution of the LIGO-Virgo-KAGRA events,” (2024), arXiv:2409.00179 [astro-ph.CO].
- [34] Kristjan Kannike, Luca Marzola, Martti Raidal, and Hardi Veermäe, “Single Field Double Inflation and Primordial Black Holes,” *JCAP* **09**, 020 (2017), arXiv:1705.06225 [astro-ph.CO].
- [35] Andrew D. Gow, Christian T. Byrnes, and Alex Hall, “Accurate model for the primordial black hole mass distribution from a peak in the power spectrum,” *Phys. Rev.*

- D **105**, 023503 (2022), arXiv:2009.03204 [astro-ph.CO].
- [36] Jens C. Niemeyer and K. Jedamzik, “Near-critical gravitational collapse and the initial mass function of primordial black holes,” *Phys. Rev. Lett.* **80**, 5481–5484 (1998), arXiv:astro-ph/9709072.
- [37] Jun’ichi Yokoyama, “Cosmological constraints on primordial black holes produced in the near critical gravitational collapse,” *Phys. Rev. D* **58**, 107502 (1998), arXiv:gr-qc/9804041.
- [38] Bernard Carr, Florian Kuhnel, and Marit Sandstad, “Primordial Black Holes as Dark Matter,” *Phys. Rev. D* **94**, 083504 (2016), arXiv:1607.06077 [astro-ph.CO].
- [39] V. De Luca, G. Franciolini, and A. Riotto, “On the primordial black hole mass function for broad spectra,” *Phys. Lett. B* **807**, 135550 (2020), arXiv:2001.04371 [astro-ph.CO].
- [40] Heling Deng, “A possible mass distribution of primordial black holes implied by LIGO-Virgo,” *JCAP* **04**, 058 (2021), arXiv:2101.11098 [astro-ph.CO].
- [41] Gerald D. Quinlan and Stuart L. Shapiro, “Dynamical Evolution of Dense Clusters of Compact Stars,” *Astrophys. J.* **343**, 725 (1989).
- [42] Hideaki Mouri and Yoshiaki Taniguchi, “Runaway merging of black holes: analytical constraint on the timescale,” *Astrophys. J. Lett.* **566**, L17–L20 (2002), arXiv:astro-ph/0201102.
- [43] Julio F. Navarro, Carlos S. Frenk, and Simon D. M. White, “A Universal Density Profile from Hierarchical Clustering,” *Astrophys. J.* **490**, 493–508 (1997), arXiv:astro-ph/9611107 [astro-ph].
- [44] William H. Press and Paul Schechter, “Formation of Galaxies and Clusters of Galaxies by Self-Similar Gravitational Condensation,” *Astrophys. J.* **187**, 425–438 (1974).
- [45] Piero Madau and Mark Dickinson, “Cosmic Star Formation History,” *Ann. Rev. Astron. Astrophys.* **52**, 415–486 (2014), arXiv:1403.0007 [astro-ph.CO].
- [46] R. Abbott *et al.* (LIGO Scientific Collaboration, Virgo Collaboration, and KAGRA Collaboration), “Population of merging compact binaries inferred using gravitational waves through gwtc-3,” *Phys. Rev. X* **13**, 011048 (2023).
- [47] LVK, “Noise curves used for simulations in the update of the observing scenarios paper,” (2020).
- [48] Miguel Zumalacárregui and Uroš Seljak, “Limits on stellar-mass compact objects as dark matter from gravitational lensing of type ia supernovae,” *Physical Review Letters* **121** (2018), 10.1103/physrevlett.121.141101.
- [49] Timothy D. Brandt, “Constraints on macho dark matter from compact stellar systems in ultra-faint dwarf galaxies,” *The Astrophysical Journal Letters* **824**, L31 (2016).
- [50] Miguel A. Monroy-Rodríguez and Christine Allen, “The end of the macho era, revisited: New limits on macho masses from halo wide binaries,” *The Astrophysical Journal* **790**, 159 (2014).
- [51] Przemek Mróz, Andrzej Udalski, Michał K. Szymański, Mateusz Kapusta, Igor Soszyński, Łukasz Wyrzykowski, Paweł Pietrukowicz, Szymon Kozłowski, Radosław Poleski, Jan Skowron, Dorota Skowron, Krzysztof Ulaczyk, Mariusz Gromadzki, Krzysztof Rybicki, Patryk Iwanek, Marcin Wrona, and Milena Ratajczak, “Microlensing optical depth and event rate toward the large magellanic cloud based on 20 yr of ogle observations,” *The Astrophysical Journal Supplement Series* **273**, 4 (2024).
- [52] Przemek Mróz, Andrzej Udalski, Michał K. Szymański, Igor Soszyński, Łukasz Wyrzykowski, Paweł Pietrukowicz, Szymon Kozłowski, Radosław Poleski, Jan Skowron, Dorota Skowron, Krzysztof Ulaczyk, Mariusz Gromadzki, Krzysztof Rybicki, Patryk Iwanek, Marcin Wrona, and Milena Ratajczak, “No massive black holes in the milky way halo,” *Nature* **632**, 749–751 (2024).
- [53] Pasquale D. Serpico, Vivian Poulin, Derek Inman, and Kazunori Kohri, “Cosmic microwave background bounds on primordial black holes including dark matter halo accretion,” *Physical Review Research* **2** (2020), 10.1103/physrevresearch.2.023204.
- [54] P. Tisserand, L. Le Guillou, C. Afonso, J. N. Albert, J. Andersen, R. Ansari, É. Aubourg, P. Bareyre, J. P. Beaulieu, X. Charlot, C. Coutures, R. Ferlet, P. Fouqué, J. F. Glicenstein, B. Goldman, A. Gould, D. Graff, M. Gros, J. Haissinski, C. Hamadache, J. de Kat, T. Lasserre, É. Lesquoy, C. Loup, C. Magneville, J. B. Marquette, É. Maurice, A. Maury, A. Milsztajn, M. Moniez, N. Palanque-Delabrouille, O. Perdureau, Y. R. Rahal, J. Rich, M. Spiro, A. Vidal-Madjar, and L. Vigroux, “Limits on the macho content of the galactic halo from the eros-2 survey of the magellanic clouds,” *Astronomy and Astrophysics* **469**, 387–404 (2007).
- [55] C. Alcock, R. A. Allsman, D. R. Alves, T. S. Axelrod, A. C. Becker, D. P. Bennett, K. H. Cook, N. Dalal, A. J. Drake, K. C. Freeman, M. Geha, K. Griest, M. J. Lehner, S. L. Marshall, D. Minniti, C. A. Nelson, B. A. Peterson, P. Popowski, M. R. Pratt, P. J. Quinn, C. W. Stubbs, W. Sutherland, A. B. Tomaney, T. Vandehei, D. L. Welch, and (The MACHO Collaboration), “Macho project limits on black hole dark matter in the 1-30 solar mass range,” *The Astrophysical Journal* **550**, L169 (2001).
- [56] Anne M. Green and Bradley J. Kavanagh, “Primordial Black Holes as a dark matter candidate,” *J. Phys. G* **48**, 043001 (2021), arXiv:2007.10722 [astro-ph.CO].
- [57] Bradley J. Kavanagh, “bradkav/pbhbounds: Release version,” (2019).
- [58] Bernard Carr, Sebastien Clesse, Juan Garcia-Bellido, Michael Hawkins, and Florian Kuhnel, “Observational evidence for primordial black holes: A positivist perspective,” *Phys. Rept.* **1054**, 1–68 (2024), arXiv:2306.03903 [astro-ph.CO].
- [59] Bradley J. Kavanagh, Daniele Gaggero, and Gianfranco Bertone, “Merger rate of a subdominant population of primordial black holes,” *Phys. Rev. D* **98**, 023536 (2018), arXiv:1805.09034 [astro-ph.CO].
- [60] Lang Liu, Zong-Kuan Guo, and Rong-Gen Cai, “Effects of the surrounding primordial black holes on the merger rate of primordial black hole binaries,” *Phys. Rev. D* **99**, 063523 (2019), arXiv:1812.05376 [astro-ph.CO].
- [61] Gabriele Franciolini, Roberto Cotesta, Nicholas Loutrel, Emanuele Berti, Paolo Pani, and Antonio Riotto, “How to assess the primordial origin of single gravitational-wave events with mass, spin, eccentricity, and deformability measurements,” *Phys. Rev. D* **105**, 063510 (2022), arXiv:2112.10660 [astro-ph.CO].